Fleeting but Not Forgotten: The Imprint of Escaping Hydrogen Atmospheres on Super-Earth Interiors

James G. Rogers , Hilke E. Schlichting , and Edward D. Young
Department of Earth, Planetary, and Space Sciences, The University of California, Los Angeles, 595 Charles E. Young Drive East, Los Angeles, CA 90095, USA
Received 2024 February 20; revised 2024 May 1; accepted 2024 May 28; published 2024 July 16

Abstract

Small, close-in exoplanets are divided into two subpopulations: super-Earths and sub-Neptunes. Most super-Earths are thought to have lost their primordially accreted hydrogen-dominated atmospheres via thermally driven winds. We consider the global chemical equilibrium of super-Earths and the lasting impacts of their fleeting hydrogen atmospheres. We find that hydrogen is efficiently sequestered into the interior, oxidizing iron and endogenously producing $\sim$0.5%–1.0% water by mass. As the atmospheres of super-Earths are continuously sculpted by mass loss and chemical equilibration, they remain hydrogen-dominated by mole (number) fraction but become steam-dominated by mass, which may be observable with JWST for planets transitioning across the radius valley. One of the main effects of efficient sequestration of hydrogen into the interior is to produce an underdense bulk interior compared to that of Earth. We predict bulk densities of super-Earths to be $\sim$5.0 g cm^{-3} for a $1M_\oplus$ planet, which is consistent with high-precision mass measurements and also population-level inference analyses from atmospheric escape models.

Unified Astronomy Thesaurus concepts: Exoplanet evolution (491); Exoplanet atmospheric evolution (2308); Exoplanet atmospheric composition (2021); Exoplanet structure (495)

1. Introduction

Hydrogen plays a central role in controlling various stages of planetary formation and evolution. For the population of small, close-in exoplanets (super-Earths and sub-Neptunes; e.g., Howard et al. 2012; Fressin et al. 2013; Silburt et al. 2015; Mulders et al. 2018; Zink et al. 2019), hydrogen-dominated gas is initially accreted from a planet's nascent protoplanetary disk to form a primordial atmosphere (e.g., Lee et al. 2014; Ginzburg et al. 2016). As the disk disperses, much of this atmosphere can be lost through a boil-off stage, in which the disk rapidly drains onto its host star, inducing extreme atmospheric escape (Owen & Wu 2016; Ginzburg et al. 2016; Rogers et al. 2024). Then, once the planet receives direct irradiation from its host star, its remaining hydrogen-dominated atmosphere is bombarded by stellar irradiation, inducing further atmospheric escape via X-ray/EUV (XUV) photoevaporation (e.g., Owen & Wu 2013; Lopez & Fortney 2013) and core-powered mass loss (e.g., Ginzburg et al. 2018; Gupta & Schlichting 2019; Rogers et al. 2024).

The loss, or retention, of hydrogen-dominated atmospheres has been used to explain various features in the exoplanet demographics accurately. Examples include the position and slope of the observed radius gap (e.g., Fulton et al. 2017; Van Eylen et al. 2018; Petigura et al. 2022) as a function of the orbital period and stellar mass (e.g., Gupta & Schlichting 2019, 2020; Rogers & Owen 2021; Rogers et al. 2021), the planet mass–radius diagram (e.g., Lopez & Fortney 2014; Chen & Rogers 2016; Kubyshkina & Fossati 2022; Rogers et al. 2023b), as well as the short orbital period Neptune desert (Owen & Lai 2018). It is also known that many sub-Neptunes require a significant hydrogen atmosphere to reproduce their observed bulk densities (e.g., Jontof-Hutter et al. 2014; Weiss & Marcy 2014; Benneke et al. 2019). Direct observational evidence also exists for the prevalence of hydrogen-dominated atmospheres in the form of Lyα and Hα transit spectroscopy (e.g., Dos Santos 2023), as well as recent atmospheric characterization of sub-Neptunes with JWST (e.g., Madhusudhan et al. 2023; Wogan et al. 2024).

A less well-explored avenue of investigation, however, is the potential impact of hydrogen-dominated atmospheres on the bulk interiors of super-Earths and sub-Neptunes (e.g., Kite et al. 2016, 2019, 2020; Chachan & Stevenson 2018; Olson & Sharp 2018; Lichtenberg 2021; Kite & Schaefer 2021; Schlichting & Young 2022; Misener et al. 2023; Suer et al. 2023; Charnoz et al. 2023). Multiple works have shown that, for hydrogen-dominated atmospheres to explain the small planet demographics, the bimodal subpopulations of super-Earths and sub-Neptunes originally began as a single population of "Earth-like" interiors hosting hydrogen-dominated atmospheres (e.g., Owen & Wu 2017; Wu 2019; Gupta & Schlichting 2019). The exact extent to which these interiors were consistent with Earth was statistically quantified in Rogers & Owen (2021) and Rogers et al. (2023a), who found that such interiors were, in fact, $\sim$10% underdense when compared to Earth's density of $\sim$5.5 g cm^{-3}. This also aligns with the precise density measurements of the TRAPPIST-1 system planets, which demonstrate similar bulk underdensities when compared to Earth (Agol et al. 2021).

Hydrogen is a highly reactive species, meaning chemical reactions with a magma ocean and core are heavily favored. Schlichting & Young (2022) used chemical equilibrium models for sub-Neptunes, comprised of metal-rich cores, silicate-rich mantles, and hydrogen-rich atmospheres, to demonstrate the overall reduction of cores and mantles and oxidation of atmospheres. They noted that hydrogen and oxygen comprised significant fractions of the metal cores at chemical equilibrium, reducing their densities. Young et al. (2023) used the same

chemical equilibrium models to argue that Earth's water content, core density deficit, and overall oxidation state can be explained by the presence of an initial hydrogen-dominated atmosphere atop progenitor Earth embryos.

In this paper, we focus on super-Earths: those planets that are stripped of their hydrogen-dominated atmosphere in the scenario of atmospheric escape, leaving behind rocky bodies with negligible atmospheric mass, sitting below the radius gap. Despite losing their hydrogen-dominated atmospheres, we show that this chemical species will have left its mark on the planetary interior. The question is, then, can the prevalence of hydrogen in the history of super-Earths explain their reported underdensities when compared to Earth? Furthermore, what are the chemical properties and abundances of the escaping atmospheres, sculpted by mass loss and chemical equilibration?

2. Method

We aim to determine the global chemical equilibrium state of super-Earths, under the assumption that they originally hosted a significant hydrogen-dominated atmosphere atop an Earth-like interior ($\sim 1/3$ metal core, $\sim 2/3$ silicate mantle, by mass, as seems likely given recent surveys of probable metal core fractions; e.g., Trierweiler et al. 2023). To do so, we utilize the chemical equilibrium model of Schlichting & Young (2022) and Young et al. (2023). Super-Earths likely form magma oceans in contact with their hydrogen-dominated primordial atmospheres during their early evolution. During this molten phase of evolution, one can assume that chemical equilibrium would have been maintained between the interior and atmosphere due to vigorous mixing and convection. However, the computational cost of our global chemical equilibrium model demands that we cannot feasibly track the state of chemical equilibrium through time. Therefore, we instead evaluate at the *time of the last global chemical equilibrium*, which we define as the point in time at which the atmosphere is no longer able to remain in chemical equilibrium with the interior due to substantial crystallization of the magma ocean. Note that finding the time of the last global chemical equilibrium is only possible for super-Earths, since they rapidly lose their hydrogen-dominated atmospheres, allowing the magma ocean to cool more and more efficiently through a diminishing atmosphere. On the other hand, the magma oceans of sub-Neptunes are likely to remain fully molten due to their large hydrogen-dominated atmospheres, preventing sufficient cooling and termination of global chemical equilibrium. To identify the time of the last global chemical equilibrium for super-Earths, we use the semianalytic atmospheric structure and evolution models of Rogers & Owen (2021), which we outline below.

2.1. Determining the Time of the Last Global Chemical Equilibrium

To find the time of the last global chemical equilibrium, we model the atmospheric evolution of a typical super-Earth. We assume a radiative–convective equilibrium model, following the works of Ginzburg et al. (2016), Owen & Wu (2017), Gupta & Schlichting (2019), Owen & Campos Estrada (2020), and Rogers & Owen (2021). These models assume an interior convective region, modeled as an adiabat of index γ with a

temperature profile (e.g., Rafikov 2006):

$$T(r) = T_{rcb}\left[1 + \nabla_{ad}\frac{GM_p}{c_s^2 R_{rcb}}\left(\frac{R_{rcb}}{r} - 1\right)\right], \qquad (1)$$

where the subscript "rcb" refers to quantities evaluated at the radiative–convective boundary. Here, $\nabla_{ad} \equiv (\gamma - 1)/\gamma$ is the adiabatic gradient and M_p is the planet's mass. Above the convective region sits a radiative layer, assumed to be isothermal at an equilibrium temperature of T_{eq}. Note that, by definition of an isothermal outer region, $T_{eq} = T_{rcb}$. The sound speed in Equation (1) is evaluated at the radiative–convective boundary, $c_s^2 \equiv k_B T_{eq}/\mu m_H$, where $\mu = 2.35$ is the mean molecular weight for an initially hydrogen-dominated atmosphere (e.g., Anders & Grevesse 1989). Note that in Section 3.1, we find that the atmospheric mean molecular weight will increase by a factor of ~ 2–4 with time due to the effects of chemical equilibrium and atmospheric escape. If the atmosphere is fully mixed all the way to the sonic point, increasing the mean molecular weight will, to first order, reduce mass-loss rates since the sound speed of escaping gas reduces. For now, we assert that this change has little effect on the results of this study, and discuss this in detail in Section 4.3. We do consider the escape of heavier species, e.g., H_2O, within atmospheres in Section 3.2.1.

We evolve models from an initial atmospheric mass fraction, defined as $X_{atm} \equiv M_{atm}/M_{interior}$, where M_{atm} is the atmospheric mass, and $M_{interior}$ is the nongaseous planet mass (typically referred to as the "core" mass in exoplanetary science). We adopt the following initial atmospheric mass fractions:

$$X_{atm,init} = 0.01\left(\frac{M_{interior}}{M_\oplus}\right)^{0.44}\left(\frac{T_{eq}}{1000\ K}\right)^{0.25}, \qquad (2)$$

from the analysis of Ginzburg et al. (2016), which accounts for initial gas accretion and boil-off during protoplanetary disk dispersal (assuming no orbital migration). The model is evolved, accounting for radiative cooling and atmospheric escape (see Rogers & Owen 2021, for details). For the latter process, we assume XUV photoevaporative mass-loss rates of:

$$\dot{M} = \eta\frac{\pi R_p^3 F_{XUV}}{GM_p}, \qquad (3)$$

where F_{XUV} is the incident stellar XUV flux (following Rogers et al. 2021), R_p is the planet's radius, and η is the mass-loss efficiency, taken from the hydrodynamic models of Owen & Jackson (2012). For simplicity, we model atmospheric mass loss by photoevaporation rather than core-powered mass loss (e.g., Ginzburg et al. 2018; Gupta & Schlichting 2019), but we stress that our results are independent of which of these two mass-loss mechanisms is assumed, given the similarities in the underlying physics (e.g., see Figure 1 of Rogers et al. 2023b). In this study, we only concern ourselves with the atmospheric masses and interior temperatures at a single point in a planet's evolution, i.e., the time of the last global chemical equilibrium in a planet's evolution, which is very similar for the two mass-loss mechanisms.

To determine the atmospheric conditions at the time of the last global chemical equilibrium, we track the temperature at

the base of the atmosphere, $T_{atm,base}$, defined as $T(r = R_{interior})$ from Equation (1). We begin our evolution models at 10 Myr, for which this base temperature can range from ~4000 to 10,000 K, depending on $M_{interior}$ and $X_{atm,init}$. As the planet thermally cools and loses mass due to atmospheric escape, $T_{atm,base}$ decreases. We define the time of the last global chemical equilibrium as the time at which the temperature at the base of the atmosphere drops $T_{atm,base} \leqslant 2000$ K, appropriate for substantial crystallization throughout a silicate melt (e.g., Andrault et al. 2011). Such crystallization is likely to halt large-scale mixing and thus prevent efficient chemical equilibrium throughout the planet. At this point, we record the atmospheric mass fraction, $X_{atm,eq}$. Then, the goal is to find a global chemical equilibrium model that results in a hydrogen atmospheric mass fraction equal to this value $X_{atm,eq}$. In other words, we assert that the global chemical equilibrium state of a planet with a hydrogen atmospheric mass fraction of $X_{atm,eq}$ is indicative of a super-Earth, bound to lose the remaining hydrogen content of its atmosphere, and for which large-scale chemical reactions between interior and atmosphere are unlikely to continue.

2.2. Evaluating Global Chemical Equilibrium

To find global chemical equilibrium, we adopt the models of Schlichting & Young (2022) and Young et al. (2023). These models use a set of linearly independent chemical reactions, including 13 phase components for the liquid mantle and core: MgO, SiO_2, $MgSiO_3$, FeO, $FeSiO_3$, Na_2O, Na_2SiO_3, Fe_{metal}, Si_{metal}, O_{metal}, H_{metal}, $H_{2,silicate}$, and $H_2O_{silicate}$; and six phase components for the atmosphere: $H_{2,gas}$, CO_{gas}, $CO_{2,gas}$, $CH_{4,gas}$, $O_{2,gas}$, and H_2O_{gas}. Reactions are allowed to take place between core and mantle, as well as between mantle and atmosphere. We list the linearly independent reactions in the Appendix, although we stress that these reactions are not the only allowed reaction pathways. Instead, they are a set of basis vectors through which other relevant reactions may occur through linear combinations of such basis vectors (see Schlichting & Young 2022, for details).

Chemical equilibrium is found by solving for the mole fraction of each species, x_i, such that for each reaction:

$$\sum_i \nu_i \, \mu_i = 0, \qquad (4)$$

where the index i is the label for each species in a reaction, ν_i is its stoichiometric coefficient, and μ_i is its chemical potential, given by:

$$\mu_i = \Delta \hat{G}_i^o + RT \ln(x_i), \qquad (5)$$

where $\Delta \hat{G}_i^o$ is the Gibbs free energy of formation at the standard state of the pure species i, corrected for pressure in the case of vapor species. Here, R is the gas constant and T is the temperature at which the reaction takes place. As discussed in detail in Schlichting & Young (2022), Equation (4) is solved for the mole fraction of each species, along with the atmospheric pressure, all with the additional constraints of conservation of mass for all elements, and a unity sum of mole fractions for all species in each phase. Numerically, we solve the system of nonlinear equations with the simulated annealing algorithm `dual_annealing` of Xiang et al. (1997), and a Monte Carlo Markov chain, specifically the `emcee` Python implementation (Foreman-Mackey et al. 2014) of the affine-

invariant ensemble sampler from Goodman & Weare (2010). Information on our adopted standard-state molar Gibbs free energies of reaction, $\Delta \hat{G}_i^o$, can be found in the appendix of Schlichting & Young (2022).

We set the reaction temperature, T in Equation (5), to 2000 K for reactions between atmosphere and silicate melt, such that the magma ocean is substantially crystallized (e.g., Andrault et al. 2011), thus preventing global chemical equilibrium via efficient mixing (see Section 2.1). Reactions between silicate melt and metal melt, on the other hand, are likely to occur at greater depths and, thus, higher temperatures. Therefore, we adopt a reaction temperature of 3000 K between silicate and metal species, as is suggested to be the case for Earth's silicate–metal equilibration (e.g., Wood 2008). The simplicity in these choices can be justified in this very first study, given the uncertainty in the interior structure of rocky super-Earths. An example of such uncertainties is that, as is the case for Earth, one may expect the metal to rain out from the silicate to form an iron-rich core due to its higher density. In this case, an adiabatic temperature profile can be used to calculate the reaction temperature between the metal and silicate species (at the core–mantle boundary, CMB). However, for the early planetary formation of super-Earths in hydrogen-rich nebulae, it remains unclear whether this core differentiation does, in fact, occur (e.g., Lichtenberg 2021). As shown in Schlichting & Young (2022) and Young et al. (2023), and as we shall demonstrate in Section 3.1, hydrogen is sequestered extremely efficiently inside the interior. Its effect will be to alter the buoyancy of both metal and silicate species, potentially changing convection, equation of state properties, and the ultimate rainout of dense metal species. Choosing the correct temperature profile is, therefore, fraught with many of these uncertainties, which we discuss further in Section 4.3.

As discussed in Section 2.1, the goal is to find a global chemical equilibrium model for which the hydrogen mass fraction in the atmosphere is equal to that which renders a magma ocean surface temperature of 2000 K, as a result of atmospheric cooling and mass loss. We refer to this hydrogen atmospheric mass fraction as $X_{atm,eq}$. We stress again that this is only possible for super-Earths, and not for sub-Neptunes, since the latter will likely retain fully molten magma oceans due to their thick hydrogen-dominated atmospheres. In our case of super-Earths, we run successive equilibrium models with increasing amounts of hydrogen already sequestered in the interior (mostly in the form of H_{metal}), as well as an initial hydrogen atmospheric mass fraction given from Equation (2), until the amount of hydrogen in its atmosphere matches $X_{atm,eq}$, with a numerical accuracy of <2%. The accepted model is, therefore, representative of a rocky super-Earth, having formed in a hydrogen-rich protoplanetary disk, subjected to atmospheric cooling and escape, until its interior no longer chemically interacts with its atmosphere.

3. Results

We model super-Earths with an atmospheric equilibrium temperature of 1000 K (assuming 0 albedo) and masses between $0.8 M_\oplus \leqslant M_p \leqslant 5.1 M_\oplus$, which encompass the range of planet masses that would have been stripped via atmospheric escape at this equilibrium temperature around a solar mass star. We assume an Earth-like interior iron mass fraction of 0.32 for all planets and a hydrogen-dominated atmosphere with only trace amounts of other gaseous species. We now present results
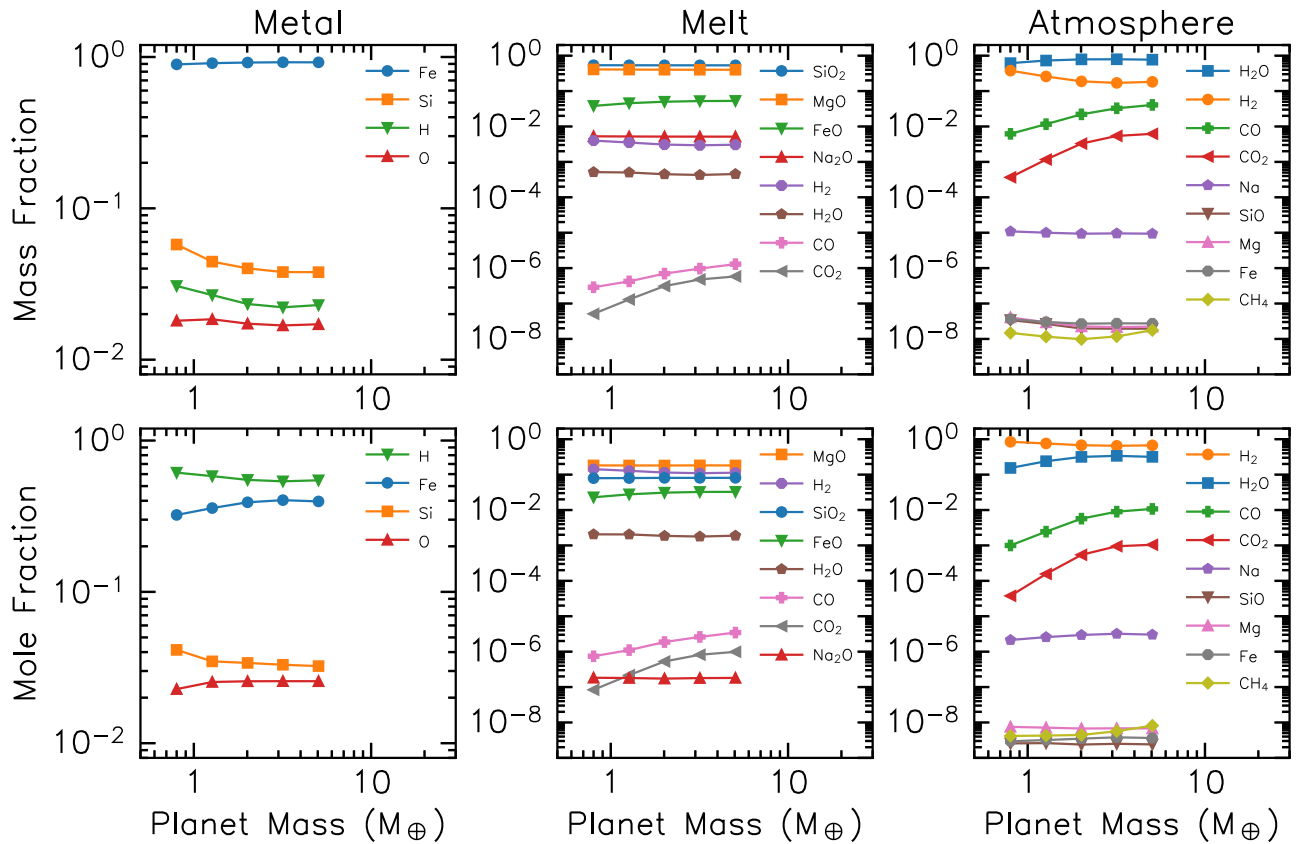
Figure 1. Chemical abundances of modeled super-Earths at the time of the last global chemical equilibrium, in terms of mass fraction and mole fraction in the top and bottom row, respectively. We show these abundances in the metal and silicate melts, and atmospheric phases for each species in the left, middle, and right-hand columns, respectively. We predict large quantities of light-element (H and O) sequestration into the metal and the production of significant quantities of H_2O in the atmosphere.

on their bulk properties and chemical makeup at the time of the last global chemical equilibrium in the following sections.

3.1. Interior and Atmospheric Chemical Compositions

We calculate the mole and mass fractions at the chemical equilibrium of each species, in each phase, which are presented in Figure 1. Abundances in the metal, silicate melt, and atmosphere are shown in the left, middle, and right-hand panels, respectively. Mass and mole fractions are shown in the top and bottom rows, respectively.

3.1.1. Interior

By mass, iron constitutes $\gtrsim$90% of the metal across the entire range in planet masses. However, in terms of mole fraction, there is approximately twice as much hydrogen than iron, the former having been sequestered into the metal as a direct result of equilibration with a hydrogen-rich atmosphere. There is also 5% Si and 2% O, by mass, as a result of reduction/oxidation reactions triggered by interactions with hydrogen. The presence of light elements in the metal leads to a metal density deficit when compared to pure iron, which is shown in the upper right-hand panel of Figure 2 (see Schlichting & Young 2022; Young et al. 2023, for details of this calculation). One can see that larger-mass planets experience a lower metal density deficit. This is because larger-mass planets host atmospheres with steeper temperature gradients in their convective envelopes, leading to less atmospheric mass being present at the time of the last global

chemical equilibrium (as defined in Section 2.1). As a result, larger-mass planets undergo the time of the last global chemical equilibrium with a smaller hydrogen mass fraction, ultimately acting as a smaller reservoir for any metal density deficit, as shown in the upper left panel of Figure 2. For reference, Earth has a measured metal density deficit of 10% (e.g., Birch 1964; Badro et al. 2015). We predict a larger deficit than Earth, which is unsurprising since Earth's final assembly likely proceeded from roughly Mars-sized embryos via a giant impact phase long after the gas disk had dissipated. Intriguingly, it was recently shown that repeating the above global chemical equilibrium calculations for Earth's progenitor embryos, does yield a density deficit consistent with Earth (Young et al. 2023).

The silicate melt mass fraction is dominated by the metal oxides SiO_2, MgO, and FeO. This is unsurprising since these species are the constituents of typical silicates such as $MgSiO_3$, $FeSiO_3$, and Na_2SiO_3. Hydrogen is present in the silicate but does not contribute a significant density deficit, unlike the metal, with mass fractions of $\lesssim$0.5% for H_2 and $\lesssim$0.05% for H_2O.

3.1.2. Atmosphere

The atmospheres of super-Earths at the time of the last global chemical equilibrium can be thought of as transient atmospheres. As an initial sub-Neptune loses its hydrogen-dominated atmosphere, physical processes will continue to sculpt the atmosphere's composition as it transitions to become
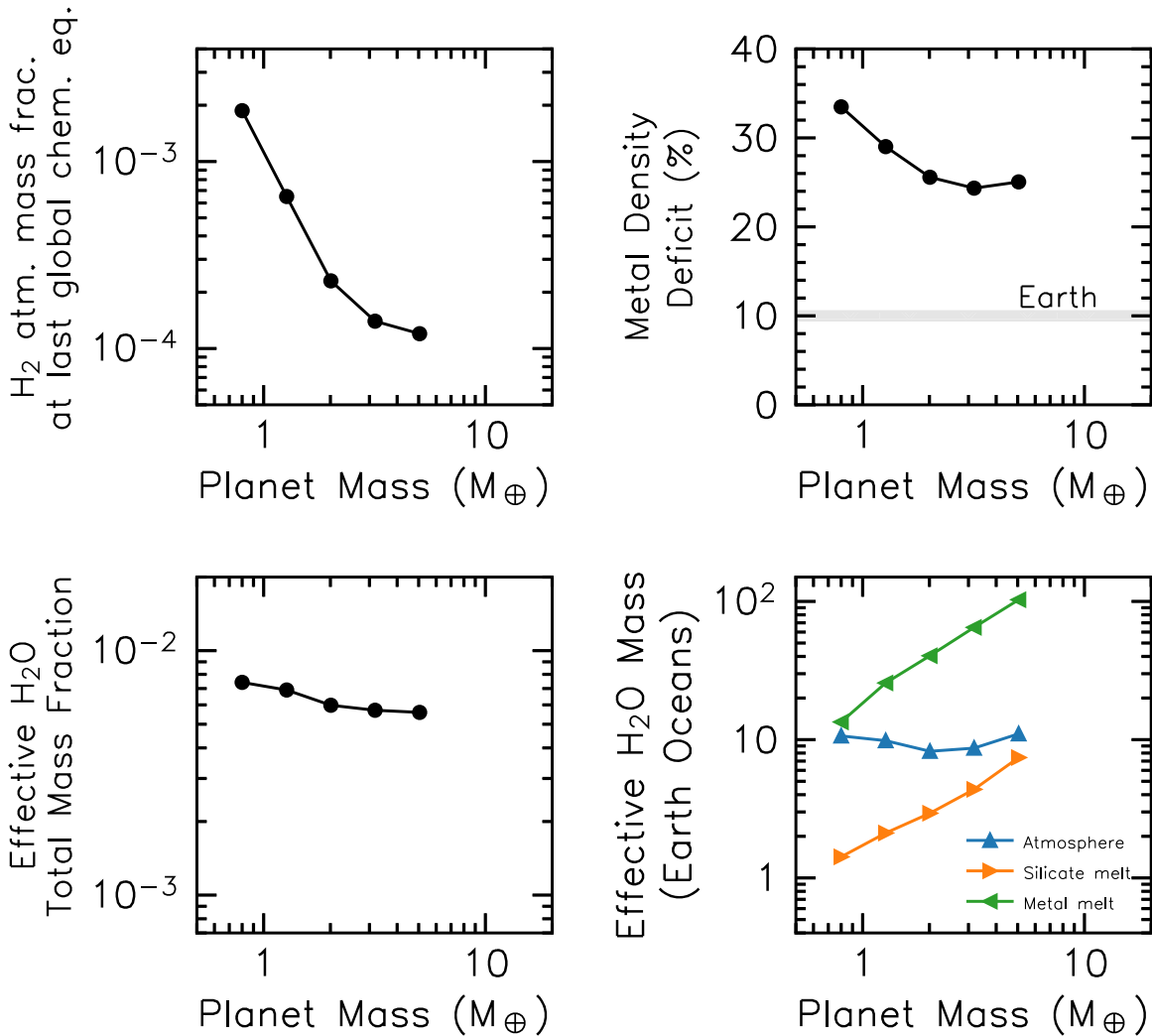
Figure 2. Upper left: H_2 atmospheric mass fraction at the time of the last global chemical equilibrium, defined as the time a super-Earth's magma ocean substantially crystallizes, thus halting large-scale chemical reactions between the interior and atmosphere. Upper right: metal density deficit, relative to pure Fe, shown for varying planet masses. For reference, this is compared to that of Earth, which has a measured metal deficit of $\sim$10% (e.g., Birch 1964; Badro et al. 2015). Lower left: total effective water mass fraction representing the amount of water endogenously produced due to chemical equilibrium with a hydrogen atmosphere. Lower right: effective water mass reservoirs, measured in Earth oceans (1.4×10^{24} g), split into individual gaseous, silicate melt, and metal phases in blue, orange, and green, respectively. Here, we consider *effective* content since molecular H_2O is very unlikely to exist, specifically in the metal core. In practice, the effective water content is calculated by pairing all O atoms in the metal phase with two H atoms. Note that, as shown in Figure 1, this pairing is oxygen-limited.

a super-Earth with a negligible atmospheric mass. Here, we present the chemical state of super-Earth atmospheres at the time of the last global chemical equilibrium, which corresponds to $\sim$a few tens of Myr. It is important to note that the final state of these atmospheres after ~ 1 Gyr of evolution will continue to be dictated by other processes, such as further atmospheric escape or outgassing, which we discuss in Sections 3.2.1 and 4.

As shown in Figure 1, we find atmospheres that are steam-dominated by the mass fraction at the time of the last global chemical equilibrium. This corresponds to hydrogen-dominated atmospheres by mole (number) fraction. Although we do not solve for chemical abundances as a function of the pressure and temperature in the atmosphere (e.g., Markham et al. 2022; Misener & Schlichting 2022; Misener et al. 2023), we do calculate mean molecular weights,[1] which range from $4.5 \lesssim \mu/m_H \lesssim 7.4$. The main driver of the increased mean

molecular weight is the production of water, which constitutes a partial pressure in the range of $\sim$40–400 bar for the planets in this study. This water reservoir is unlikely to condense out into an ocean phase since these planets exist at such extreme equilibrium temperatures, thus precluding the ability for the steam to cool. Apart from the residual H_2, the most abundant atmospheric species by mole fraction after H_2O are CO and CO_2, present at the $\sim$0.01%–1% level by atmospheric mass, with CO/CO_2 number ratios of $\sim$20. We note here that this relative ratio of CO/CO_2 is only representative in the deep atmosphere as photochemistry is expected to alter this ratio in the upper atmosphere, which can be probed observationally. Trace amounts of the remaining gas constituents, such as SiO and CH_4, are also present. Note that O_2 is not included in Figure 1, due to its very low abundance of $\sim 10^{-11}$ by mole fraction. As discussed, we do not consider the atmospheric structure and resultant variation in chemical abundances as a function of the pressure and temperature above the planet's surface, as done in Markham et al. (2022), Misener &

---

[1] To calculate the atmospheric mean molecular weight, we only consider H_2, H_2O, CO, CO_2, CH_4, and O_2 species, since the remaining gas species would condense out and not be observable in the upper atmosphere.

Schlichting ([2022](#)), and Misener et al. ([2023](#)). This added complexity is beyond the scope of this work and is left for future study.

3.1.3. Global Water Content

As discussed, Figure [2](#) shows the H_2 atmospheric mass fraction at the time of the last global chemical equilibrium, as well as the metal density deficit in the Fe core in the top left and top right panels, respectively. In addition, we also show the global water content of super-Earths, both as a total mass fraction and also split between the metal, silicate melt, and atmospheric components in the bottom left and bottom right panels, respectively. Note that, although it is commonplace to discuss the interior water content of planets (e.g., Dorn & Lichtenberg [2021](#)), H_2O is very unlikely to exist in molecular form within the deep interior, particularly in the iron core. Instead, H and O will exist in atomic form (hence our speciation in Figure [1](#)). Nevertheless, we compute the total *effective* water content of the planet in each phase for comparison. In the case of the metal core, this is performed by pairing oxygen atoms with two hydrogen atoms until the oxygen reservoir is depleted. One can see that super-Earths host $\sim$0.5%–1.0% H_2O by mass as a direct result of chemical equilibrium with a hydrogen-dominated atmosphere. We refer to this as *endogenously* produced water. Most of this effective water content is stored in the metal core, with approximately an order of magnitude less in the mantle, as shown in the bottom right panel of Figure [2](#). The atmosphere, on the other hand, stores an intermediate amount of water in the form of steam (although this is likely removed during further atmospheric escape; see Section [3.2.1](#)). The atmosphere holds $\sim$10 Earth oceans of H_2O, which is independent of planet mass due to the approximate balance of competing effects: on one hand, larger planets host a larger reservoir of chemical reactants to produce water; on the other hand, larger super-Earths also retain smaller H_2 atmospheres at the time of the last global chemical equilibrium, as shown in the top left panel of Figure [2](#).

3.1.4. Oxygen Fugacity

In addition to chemical abundances, we also compute the oxygen fugacity f_{O_2} of the magma ocean and atmosphere. Fugacity measures the partial pressure of oxygen that would be in equilibrium with the system and is, therefore, a convenient measure of a material's oxidation state at equilibrium. Historically, this is measured relative to the reaction in which pure iron is oxidized to form pure FeO (iron wüstite, IW), $Fe + 1/2\ O_2 = FeO$. When reported as deviations from the IW reference, on a logarithmic scale, the oxygen fugacity is reported as:

$$\Delta IW = 2 \log\left(\frac{x_{FeO}}{x_{Fe}}\right), \tag{6}$$

where x_i refers to a mole fraction of FeO in the silicate melt or Fe in the metal. As with the issue of *effective* molecular H_2O in the metal core (as described above), molecular H_2 is very unlikely to exist in the melt. Instead, atomic hydrogen will exist in the silicate crystals and oxides in polymer form. Therefore, the fugacity of the magma ocean is a measure of the partial pressure of O_2, if it indeed existed. Following this convention, we find that the fugacities of our super-Earth's magma oceans
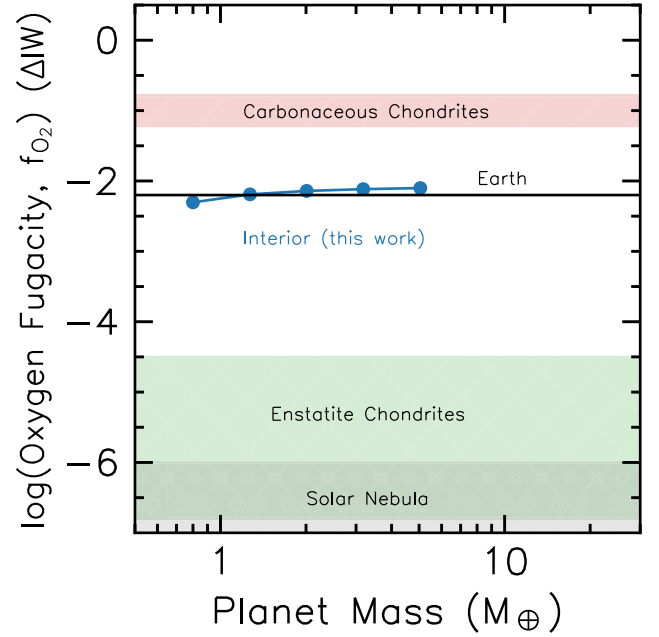

Figure 3. The oxygen fugacity of the silicate melt is shown for varying super-Earth masses in blue. Fugacity is measured relative to the FeO (Iron Wüstite, IW) buffer. We compare these to the values for Earth (Doyle et al. [2019](#)), as well as carbonaceous chondrites (red-shaded region), enstatite (E) chondrites (green-shaded region), and the Solar nebula (gray-shaded region).

are remarkably similar to that of Earth, which has a value of $\Delta IW \approx -2.2$ (Doyle et al. [2019](#)), as shown in Figure [3](#). This was also found in Young et al. ([2023](#)) when considering the chemical equilibrium of a proto-Earth and is explained due to the oxidation of Fe displaced from the core by Si. Overall, we see an increase in the oxidation state of the magma ocean from that of the solar-like nebula and E chondrites to that of Earth, purely due to the chemical equilibrium of a magma ocean with a hydrogen atmosphere. Despite the apparent contradiction of hydrogen (a reductant) causing the net oxidation of the interior, this is, in fact, due to the reduction of Si, causing a balancing oxidation of Fe (Schlichting & Young [2022](#); Young et al. [2023](#)).

3.2. Mass–Radius Relations and Bulk Densities

In this section, we compare our models with observations of super-Earths. We begin with a prescription for determining mass–radius relations, followed by an outline of our data selection and analysis.

3.2.1. Determining Mass–Radius Relations

We calculate planetary radii by following Rogers & Seager ([2010](#)) and solving for the radius $r(m)$ and pressure $P(m)$ of a spherically symmetric body in hydrostatic equilibrium as a function of the interior mass, m:

$$\frac{\partial r}{\partial m} = \frac{1}{4\pi r^2 \rho}, \tag{7}$$

$$\frac{\partial P}{\partial m} = -\frac{Gm}{4\pi r^4}, \tag{8}$$

where ρ is the density, given by an equation of state:

$$\rho = f(P, T), \qquad (9)$$

which relates the density to the pressure P and temperature T within each layer. For each planet of mass M_p, we integrate Equations (7) and (8) from $0 \leqslant m \leqslant M_p$ and impose inner boundary conditions of $r(m=0)=0$ and $P(m=0)=P_c$, where P_c is the central pressure. We solve for P_c, which yields a planet size, such that $P(m=M_p)=P_{atm}$. We integrate Equations (7) and (8) with `scipy.integrate.sol-ve_ivp` and solve for the planet radius with `scipy.optimize.newton` (Virtanen et al. 2020) with fractional tolerances of 10^{-8}.

We assume that, after Gyrs of evolution, planets will have formed differentiated iron-rich cores (an assumption that we question in Section 4.1). As such, we use a temperature-independent equation of state for Fe from Schlichting & Young (2022), following Seager et al. (2007) and Anderson et al. (2001). For the silicate melt, we use the Mg-perovskite third-order Birch–Murnaghan equation of state of Karki et al. (2000), as described in Seager et al. (2007). We assume an Earth-like iron-core mass fraction of 0.32, incorporating a metal density deficit relative to pure iron. This arises from the sequestration of light species such as hydrogen and oxygen, reducing the overall density of the metal core. We determine the metal density deficit for each model (as shown in Figure 2) and calculate the planet's radius at the base of the atmosphere.

The presence of an atmosphere, if sufficiently optically thick, will also contribute to a planet's size. Indeed, the atmospheric masses of our modeled super-Earths at the time of the last global chemical equilibrium (occurring at $\sim$a few tens of Myr) are sufficient to produce a small increase in planet size. However, the atmosphere of a super-Earth observed after Gyr of evolution is expected to be smaller in mass than those at the time of the last global chemical equilibrium. This is because atmospheric escape, driven through photoevaporative and/or bolometrically driven outflows, will continue to erode the atmosphere. In particular, escaping hydrogen, which is the lightest and easiest to liberate from the planet, can drag heavier species along with it. One can justify this with a simple calculation of the crossover mass m_c, which represents an estimate of the maximum atomic/molecular mass species that can be dragged along within the hydrogen outflow (e.g., Hunten et al. 1987; Chassefière 1996; Luger & Barnes 2015):

$$m_c = m_{H_2} + \frac{k_B T}{4\pi b \, m_{H_2} G M_p} \dot{M}_{H_2}. \qquad (10)$$

Here, m_{H_2} is the molecular mass of H_2, T is the temperature of the outflow,[2] $b \approx 4.8 \times 10^{17} (T/K)^{0.75}$ cm^{-1} s^{-1} is the binary diffusion coefficient for the two species (Zahnle & Kasting 1986), and $\dot{M}_{H_2}$ is the hydrogen mass-loss rate. For the super-Earths considered in this study, and in the simpler case of a bolometrically heated, neutral, isothermal outflow for which we set the outflow temperature equal to T_{eq} (as is the case for core-powered mass loss; e.g., Owen & Schlichting 2024),

mass-loss rates are approximated using a Parker wind model:

$$\dot{M}_{H_2} = 4\pi R_B^2 c_s \rho_{rcb} \exp\left\{ \frac{3}{2} - \frac{2R_B}{R_{rcb}} \right\}, \qquad (11)$$

where $R_B \equiv G M_{interior}/2c_s^2$ is the Bondi radius. For the super-Earths considered in this study, Equation (11) yields typical hydrogen mass-loss rates of $\dot{M}_H \sim 10^{11}$ g s^{-1} at the time of the last global chemical equilibrium (see Figure 6 from Misener & Schlichting 2021). In these cases, one attains crossover masses of order $m_c \sim 10^2$–$10^4 m_H$, which are significantly larger in mass than any gas species within the atmosphere. We use the semianalytic crossover mass prescription from Luger & Barnes (2015) to estimate the evolution of each super-Earth modeled in this paper, including crossover mass and escape rates for H_2 and H_2O. In case of a bolometrically heated, neutral, isothermal outflow, we confirm that the final atmospheric mass fractions of our super-Earths are $\lesssim 10^{-5}$, rendering a sufficiently small atmospheric optical depth so as not to increase the planet's size. While these simple calculations are informative, they ignore effects such as XUV ionization and the complex cooling processes of molecular species in optically thin outflows. In an ionized outflow, higher mean molecular weight species have an increased collisional cross section (e.g., Geiss et al. 1970; Joselyn & Holzer 1978; Geiss 1982), which allows such species to be dragged more efficiently within the outflow. This suggests that heavier species are likely lost at a higher rate than estimated using the crossover mass calculations discussed above once the contribution from ionizing radiation is considered self-consistently. Understanding these processes in more detail requires hydrodynamic modeling in the context of multiple chemical and ionized species under high-energy irradiation environments, which will then allow for robust predictions of the final state of super-Earth atmospheres, which is beyond the scope of this work.

3.2.2. Data Selection and Comparison

We compare our models with a high-fidelity sample of super-Earths with reliably measured masses and radii. We begin with the `PlanetS` catalog (Otegi et al. 2020), which selects planets based on various reliability and precision conditions. Planets in this catalog have relative mass and radius uncertainties of less than 25% and 8%, respectively. From there, we define a super-Earth to exist below the radius valley. Since the exact definition of the radius valley varies within the literature, we take a conservative approach. From Ho et al. (2024), in which short-cadence Kepler photometry was used to produce a high-precision sample of transiting exoplanets $\lesssim 4R_\oplus$, the valley is inferred to follow:

$$\log\left(\frac{R_p}{R_\oplus}\right) = A \log\left(\frac{P}{1 \text{ day}}\right) + B \log\left(\frac{M_*}{M_\odot}\right) + C, \qquad (12)$$

where $A = -0.09^{+0.02}_{-0.03}$, $B = 0.21^{+0.06}_{-0.07}$, $C = 0.35^{+0.02}_{-0.03}$. Note the importance of defining the valley as a function of the orbital period P and stellar mass M_* due to its well-documented dependencies (e.g., Berger et al. 2020; Gupta & Schlichting 2020; Rogers et al. 2021; Petigura et al. 2022). We calculate the lower boundary of the valley by resampling Equation (12) within its 1σ uncertainties 10^7 times. The lower

---

[2] The outflow temperature can range from approximately the equilibrium temperature T_{eq} in a bolometrically heated outflow, to $\sim 10^4$ K in a photoevaporative outflow (e.g., Murray-Clay et al. 2009; Schulik & Booth 2023; Owen & Schlichting 2024).
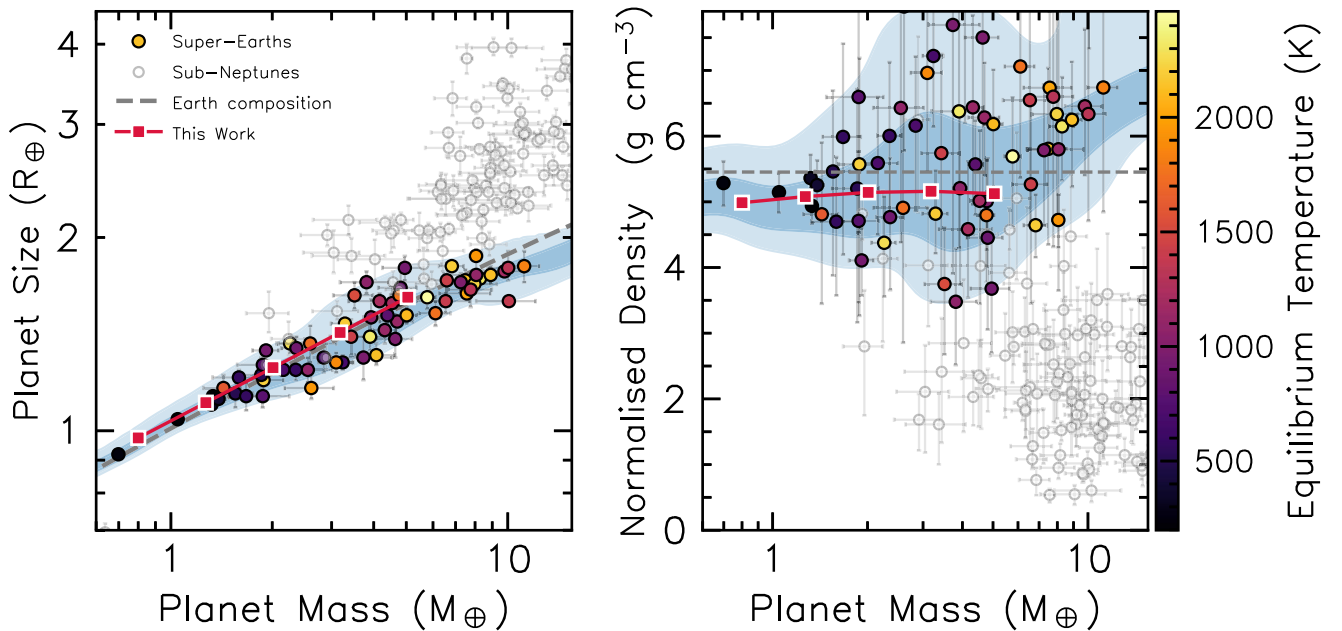
Figure 4. Our super-Earth models are shown in pink squares, compared with a sample of observed exoplanets from the `PlanetS` catalog (Otegi et al. 2020) with masses and radii constrained to 25% and 8%, respectively. In the left-hand panel, we show the mass–radius diagram, whereas, in the right-hand panel, we show normalized density as a function of the planet mass, which is the density of each planet when scaled to be $1 M_\oplus$. Gray dashed lines represent an Earth-like density of ~ 5.5 g cm^{-1}. The blue-shaded regions represent the 1σ and 2σ ranges in radius and density for the population of super-Earths, as laid out in Section 3.2.2.

1σ surface of these samples then defines the lower boundary as a function of the orbital period and stellar mass. We define a super-Earth as a planet that sits below the lower boundary, thus removing planets potentially sitting within the radius valley, whose physical properties are currently unclear. The only exceptions to this classification scheme are TRAPPIST-1 planets, which are misclassified as sub-Neptunes under this scheme despite being terrestrial in nature (Agol et al. 2021),[3] and GJ 367 b, which is consistent with a density of pure iron and hence considered an outlier (Lam et al. 2021; Goffo et al. 2023). As a result, we remove this planet from our sample.

We calculate each planet's *normalized density* (often referred to as "compressed"), which is a planet's density if it has the same mass as Earth. In other words, planets that are overdense when compared to Earth sit above ~ 5.5 g cm^{-3}, and vice versa. For this comparison, we define an Earth-like composition to have a 32% iron mass fraction with a constant 10% metal density deficit (Birch 1964; Badro et al. 2015). We then create a uniform grid in planet mass versus normalized density space and use a Gaussian kernel density estimator to determine the probability density function of the observed planets within this space. We normalize each grid slice, i, in planet mass, $M_{p,i}$, to contain equal probability density such that information is evenly spaced across the planet mass domain. Then, and again for each slice in planet mass $M_{p,i}$, we find the 1σ and 2σ contours for super-Earth normalized densities. These are presented in the right-hand panel of Figure 4 as blue contours. The left-hand panel also contains the same contours converted to the mass–radius plane. Super-Earths, as classified in the discussion above, are shown as circles, colored with their equilibrium temperature (assuming zero albedo). Sub-Neptunes are shown in gray. The 1σ and 2σ contours indicate a tentative

underdensity of super-Earths, which is consistent with the inference analysis of Rogers & Owen (2021). Our super-Earth models are shown in pink squares, which demonstrate an underdensity when compared to Earth, due to hydrogen and oxygen sequestration into the metal core. The consistency with the data suggests that primordial hydrogen atmospheres interacting with young molten interiors provide a possible explanation for a density deficit in the super-Earth population.

4. Discussion

This study has demonstrated the lasting effects of hydrogen on super-Earth interiors and atmospheres under the assumption that they initially hosted H_2-dominated atmospheres, which were then lost due to atmospheric escape. We now discuss the implications of these results and the possibility of observational tests.

4.1. Do Metal Cores Differentiate?

As additionally shown in Schlichting & Young (2022) and Young et al. (2023), we also find that hydrogen is efficiently sequestered into the interior of low-mass exoplanets in the presence of hydrogen atmospheres. Figure 1, in fact, demonstrates that hydrogen atoms outnumber iron by a factor of ~ 2 within the metal. These results, including the water production as discussed in Section 3.1, are in agreement with high $P - T$ experimental results from Horn et al. (2023) and Piet et al. (2023). From a geocentric view, one would expect iron species to rain out from the silicate melt over time to eventually form a metal core. However, the abundance of hydrogen may change this picture. Its presence, and willingness to bond with iron, may change the overall buoyancy within the melt, thus potentially delaying or even stopping metal rainout in the interior. This was highlighted in Lichtenberg (2021), who showed that this "rainout quenching" is also controlled by the iron droplet size and the internal heat flux of the mantle. We

---

[3] This misclassification arises from extrapolating the radius valley definition from Equation (12) to very low stellar masses, such as that for TRAPPIST-1.

stress that our chemical equilibrium calculations do not include an interior structure model. It is, therefore, beyond the scope of this work to self-consistently model the evolving rainout process in detail, including the solidification of the magma ocean below its surface. Nevertheless, the abundance of hydrogen may have other impacts on the global properties of the planet, such as changes in the efficiency of a potential dynamo mechanism and thus the prevalence of large-scale magnetic fields on super-Earths (e.g., Zhang & Rogers 2022).

4.2. Observational Tests

It is well-documented that attempting to discern a planet's interior structure is fraught with degeneracies when only observing planetary masses and radii (e.g., Rogers 2015; Bean et al. 2021; Rogers et al. 2023b). Unsurprisingly, then, our population-level prediction of bulk underdensities, when compared to Earth (see Figure 4), does not constitute direct observational evidence of hydrogen sequestration. Additional mechanisms to produce bulk underdensities include a planet hosting a reduced iron mass fraction (as may be the case for older planets around metal-poor stars; e.g., Trierweiler et al. 2023), or an increased initial volatile mass fraction.

On the other hand, we also predict that super-Earths will enter a phase in which their atmospheres are steam-dominated by mass (although hydrogen-dominated by mole fraction) as a result of global chemical equilibration and atmospheric escape (see Section 3.1.2). This is similar to the conclusions of Kite & Schaefer (2021). Perhaps the most interesting targets to detect such atmospheres are planets found inside the radius gap, since they may be in the process of transitioning from being a sub-Neptune to a super-Earth. In the era of atmospheric characterization of small planets with observatories such as JWST, it may be possible to detect such signatures in the coming years. We stress again, however, that further work is needed to understand how such atmospheres would evolve after the time of the last global chemical equilibrium due to cooling, mass loss, and outgassing. Furthermore, our chemical equilibrium models do not consider the variation of atmospheric chemical abundances with pressure and temperature, as was done in Markham et al. (2022), Misener & Schlichting (2022), and Misener et al. (2023).

4.3. Model Assumptions and Uncertainties

In solving for global chemical equilibrium, we have made several simplifying assumptions in our model. One such assumption is that global chemical equilibrium is maintained within and between the interior and atmosphere via efficient bulk transport, convection, and mixing until the time of the last global chemical equilibrium (e.g., Lichtenberg 2021; Salvador & Samuel 2023). Although this is likely a reasonable first approximation, it would be desirable to relax this assumption in future work by coupling an evolving interior structure model (e.g., Curry et al. 2024) with our chemistry model. This would allow one to track the cooling and crystallization of silicates as a function of the pressure and temperature, leading to the locking of volatiles inside the interior as a function of time.

As discussed in Section 2.1, we have assumed the silicate melt and atmosphere chemically equilibrate at 2000 K, whereas the silicate melt and metal equilibrate at 3000 K at the time of the last global chemical equilibrium for all super-Earths. These temperatures are sensibly chosen to ensure significant magma ocean crystallization such that efficient bulk transport and chemical equilibration are significantly suppressed beyond this point in time (e.g., Stixrude 2014; Salvador & Samuel 2023). The silicate-atmosphere temperature of 2000 K was chosen under the assumption that the magma ocean will solidify from the bottom up, in which case a surface temperature closer to the adiabatic silicate melt solidus ∼1500 K would imply the vast majority of the mantle has already solidified and chemical equilibrium has already ceased. The higher value of 2000 K thus captures the time at which the bulk of the magma ocean is in the process of crystallizing. In a similar manner, we have chosen a silicate–metal reaction temperature of 3000 K, which is lower than that predicted by an adiabatic silicate melt at the core–mantle boundary (e.g., Stixrude 2014). This is because we cannot assume the silicate melt and metal equilibrate at this temperature, especially when the planet is young and a differentiated core has not necessarily formed. This simplification, however, ignores the pressure dependence on the solidus/liquidus of an adiabatic silicate melt, which would introduce a planet mass dependence on these temperatures. As shown in Schlichting & Young (2022), the temperature at which reactions take place can change the degree of light-element sequestration in the interior. Although exploring the effects of varying reaction temperatures is beyond the scope of this work, one would expect higher temperatures to result in more light elements being sequestered into the metal core (see Figure 12 from Schlichting & Young 2022). Sequestration is also affected by the adopted H_2O solubilities (see Schlichting & Young 2022), which affect the partitioning of water into the interior (e.g., Moore et al. 1998; Dorn & Lichtenberg 2021; Bower et al. 2022). Nevertheless, we confirmed that the general result of light-element sequestration and water production is robust to minor changes in the exact H_2O solubilities. As with the previous point, evolving structure models are required to self-consistently determine how efficiently the interior allows for global chemical equilibrium (e.g., Curry et al. 2024) as a planet evolves and cools.

Finally, in Section 2.1, we assumed that we can ignore, to first order, the increase in the atmospheric mean molecular weight from $\mu = 2.35$ to $4.5 \lesssim \mu/m_H \lesssim 7.4$, as found in Section 3.1.2, in our atmospheric escape models. As previously discussed, if the atmosphere is fully mixed all the way up to the sonic point, then increasing the mean molecular weight reduces mass-loss rates due to a decreased sound speed. However, since we are only concerned with the conditions of the last global chemical equilibrium in this study, this change is unimportant in setting the hydrogen mass fraction, $X_{atm,eq}$, that renders a magma ocean surface temperature of 2000 K, as considered here. In other words, changing mass-loss rates may alter the exact time at which the last global chemical equilibrium occurs, but the value of $X_{atm,eq}$, which sets the conditions for chemical equilibrium (see Section 2.2) remains approximately the same. As highlighted in Section 3.2.1, the details of atmospheric escape in the presence of heavier gas species are complex and warrant further detailed study since the level of mixing and the resulting mean molecular weight at various heights in the atmosphere need to be modeled self-consistently with mass loss. We, therefore, leave coupled models of atmospheric escape and chemical equilibrium for future work.

5. Conclusions

The likely fate of super-Earths is to have their primordial hydrogen-dominated atmospheres removed via thermally driven atmospheric escape (e.g., Lopez & Fortney 2013; Owen & Wu 2013). In this study, we consider the effects of such mass loss, combined with global chemical equilibrium, in order to understand the bulk and chemical properties of super-Earths. To do so, we use the models of Schlichting & Young (2022) and Young et al. (2023) to evaluate the chemical state of planets at the *time of the last global chemical equilibrium*, defined as the time at which large-scale chemical interactions cease to occur between an atmosphere and planetary interior due to significant crystallization of a magma ocean. Our conclusions are as follows:

1. The net result of chemical equilibration is the efficient sequestration of hydrogen into the planetary interior. This produces bulk densities of $\sim 5.0 \, \mathrm{g \, cm^{-3}}$ when compared to Earth's density of $5.5 \, \mathrm{g \, cm^{-3}}$. This arises due to light elements, such as hydrogen and oxygen, found in the metal phase as they oxidize iron. This produces metal density deficits of 20%–40%. We show that these bulk densities are consistent with the exoplanet population and evolution inference analysis from Rogers & Owen (2021).

2. A by-product of hydrogen interactions with the interior is the production of significant quantities of water, up to ~ 0.5%–1% of a planet's mass. This equates to tens, to hundreds of Earth oceans being present within super-Earths, produced entirely through endogenous means. The water exists predominantly as a reservoir in the metal phase (in the form of separated oxygen and hydrogen), but also in the atmosphere and magma ocean to a lesser extent.

3. As a super-Earth loses its hydrogen-dominated atmosphere, its remaining atmosphere will become steam-dominated by mass (although still hydrogen-dominated by mole fraction) as a result of chemical equilibration (see also Kite & Schaefer 2021). We evaluate the chemical abundances of super-Earth atmospheres at the time of the last global chemical equilibrium, which demonstrates mean molecular weights of $4.5 \lesssim \mu/m_{\mathrm{H}} \lesssim 7.4$. Carbon-bearing species such as CO and CO_2 are also expected to be present at ~ 0.01%–1% by mass at this time. We stress that this atmosphere represents a single snapshot during a super-Earth's evolution and will inevitably be sculpted by further mass loss and outgassing. Nevertheless, these transient, steam-dominated atmospheres may be observable for planets transitioning across the radius valley with current observational facilities.

4. We speculate as to the interior structure of super-Earths, specifically whether metal cores will, in fact, differentiate as in the case of Earth. The abundance of light species, such as hydrogen and oxygen, may affect the buoyancy and rainout of metal within the magma ocean, as also discussed in Lichtenberg (2021), Schlichting & Young (2022).

We emphasize that our calculations are meant as a first attempt to understand the chemical state of super-Earths in the context of thermal and mass-loss evolution. Indeed, many approximations have bee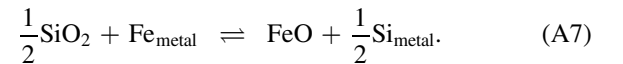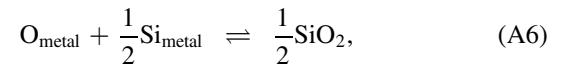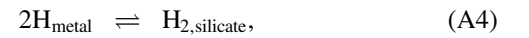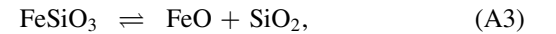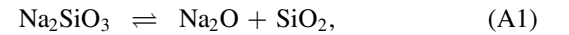n made in this work in an attempt to simplify the problem. Future work is needed on many fronts to improve our understanding of these planets. For example, coupling atmospheric evolution models with interior structure models with the necessary chemistry in a self-consistent manner will allow one to examine the sequestration process with time. Furthermore, solving for the atmospheric abundances as a function of the pressure and temperature allows for more accurate predictions for atmospheric characterization (see Markham et al. 2022; Misener & Schlichting 2022; Misener et al. 2023). Finally, more work is needed on the experimental (e.g., Horn et al. 2023; Piet et al. 2023) and ab initio calculations (e.g., Gilmore & Stixrude 2019) to better understand equations of state, miscibility and solubility properties of various species, such as iron, hydrogen, water, and silicates, under high pressures and temperatures.
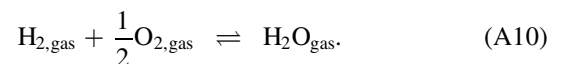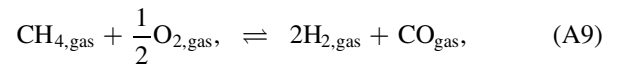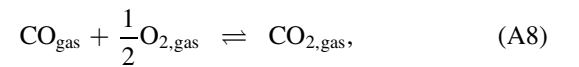
Appendix
Chemical Reactions

Our chemical equilibrium model relies on a set of linearly independent reactions, which are discussed in detail in Schlichting & Young (2022). Here, we list the reaction set, which spans our reaction space, allowing for all available pathways for our chosen species. First, speciation within the magma ocean:

$$Na_2SiO_3 \;\rightleftharpoons\; Na_2O + SiO_2, \tag{A1}$$

$$MgSiO_3 \;\rightleftharpoons\; MgO + SiO_2, \tag{A2}$$

$$FeSiO_3 \;\rightleftharpoons\; FeO + SiO_2, \tag{A3}$$

$$2H_{\mathrm{metal}} \;\rightleftharpoons\; H_{2,\mathrm{silicate}}, \tag{A4}$$

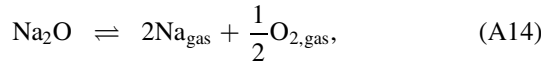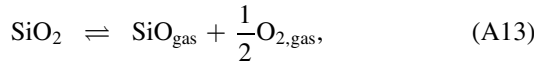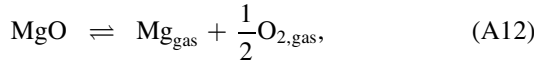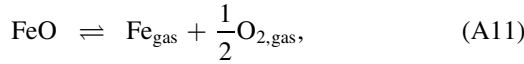$$2H_2O_{\mathrm{silicate}} + Si_{\mathrm{metal}} \;\rightleftharpoons\; SiO_2 + 2H_{2,\mathrm{silicate}}, \tag{A5}$$

$$O_{\mathrm{metal}} + \frac{1}{2}Si_{\mathrm{metal}} \;\rightleftharpoons\; \frac{1}{2}SiO_2, \tag{A6}$$

$$\frac{1}{2}SiO_2 + Fe_{\mathrm{metal}} \;\rightleftharpoons\; FeO + \frac{1}{2}Si_{\mathrm{metal}}. \tag{A7}$$

Then, reactions within the atmosphere:

$$CO_{\mathrm{gas}} + \frac{1}{2}O_{2,\mathrm{gas}} \;\rightleftharpoons\; CO_{2,\mathrm{gas}}, \tag{A8}$$

$$CH_{4,\mathrm{gas}} + \frac{1}{2}O_{2,\mathrm{gas}}, \;\rightleftharpoons\; 2H_{2,\mathrm{gas}} + CO_{\mathrm{gas}}, \tag{A9}$$

$$H_{2,\mathrm{gas}} + \frac{1}{2}O_{2,\mathrm{gas}} \;\rightleftharpoons\; H_2O_{\mathrm{gas}}. \tag{A10}$$

Finally, reactions between the atmosphere and magma ocean:

$$FeO \rightleftharpoons Fe_{gas} + \frac{1}{2}O_{2,gas}, \qquad (A11)$$

$$MgO \rightleftharpoons Mg_{gas} + \frac{1}{2}O_{2,gas}, \qquad (A12)$$

$$SiO_2 \rightleftharpoons SiO_{gas} + \frac{1}{2}O_{2,gas}, \qquad (A13)$$

$$Na_2O \rightleftharpoons 2Na_{gas} + \frac{1}{2}O_{2,gas}, \qquad (A14)$$

$$H_{2,gas} \rightleftharpoons H_{2,silicate}, \qquad (A15)$$

$$H_2O_{gas} \rightleftharpoons H_2O_{silicate}, \qquad (A16)$$

$$CO_{gas} \rightleftharpoons CO_{silicate}, \qquad (A17)$$

$$CO_{2,gas} \rightleftharpoons CO_{2,silicate}. \qquad (A18)$$
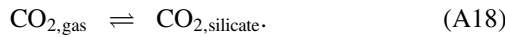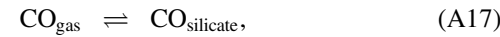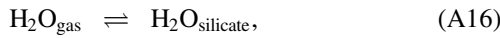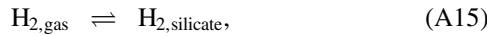
ORCID iDs

James G. Rogers ⬤ https://orcid.org/0000-0001-7615-6798
Hilke E. Schlichting ⬤ https://orcid.org/0000-0002-0298-8089
Edward D. Young ⬤ https://orcid.org/0000-0002-1299-0801

References

Agol, E., Dorn, C., Grimm, S. L., et al. 2021, PSJ, 2, 1
Anders, E., & Grevesse, N. 1989, GeCoA, 53, 197
Anderson, O. L., Dubrovinsky, L., Saxena, S. K., & LeBihan, T. 2001, GeoRL, 28, 399
Andrault, D., Bolfan-Casanova, N., Nigro, G. L., et al. 2011, E&PSL, 304, 251
Badro, J., Brodholt, J. P., Piet, H., Siebert, J., & Ryerson, F. J. 2015, PNAS, 112, 12310
Bean, J. L., Raymond, S. N., & Owen, J. E. 2021, JGRE, 126, e06639
Benneke, B., Knutson, H. A., Lothringer, J., et al. 2019, NatAs, 3, 813
Berger, T. A., Huber, D., van Saders, J. L., et al. 2020, AJ, 159, 280
Birch, F. 1964, JGR, 69, 4377
Bower, D. J., Hakim, K., Sossi, P. A., & Sanan, P. 2022, PSJ, 3, 93
Chachan, Y., & Stevenson, D. J. 2018, ApJ, 854, 21
Charnoz, S., Falco, A., Tremblin, P., et al. 2023, A&A, 674, A224
Chassefière, E. 1996, JGR, 101, 26039
Chen, H., & Rogers, L. A. 2016, ApJ, 831, 180
Curry, A., Booth, R., Owen, J. E., & Mohanty, S. 2024, MNRAS, 528, 4314
Dorn, C., & Lichtenberg, T. 2021, ApJL, 922, L4
Dos Santos, L. A. 2023, in IAU Symp. 370, Winds of Stars and Exoplanets, ed. A. A. Vidotto, L. Fossati, & J. S. Vink (Cambridge: Cambridge Univ. Press), 56
Doyle, A. E., Young, E. D., Klein, B., Zuckerman, B., & Schlichting, H. E. 2019, Sci, 366, 356
Foreman-Mackey, D., Hogg, D. W., & Morton, T. D. 2014, ApJ, 795, 64
Fressin, F., Torres, G., Charbonneau, D., et al. 2013, ApJ, 766, 81
Fulton, B. J., Petigura, E. A., Howard, A. W., et al. 2017, AJ, 154, 109
Geiss, J. 1982, SSRv, 33, 201
Geiss, J., Hirt, P., & Leutwyler, H. 1970, SoPh, 12, 458
Gilmore, T., & Stixrude, L. P. 2019, AGUFM, 2019, MR23B–0107
Ginzburg, S., Schlichting, H. E., & Sari, R. 2016, ApJ, 825, 29
Ginzburg, S., Schlichting, H. E., & Sari, R. 2018, MNRAS, 476, 759
Goffo, E., Gandolfi, D., Egger, J. A., et al. 2023, ApJL, 955, L3
Goodman, J., & Weare, J. 2010, CAMCS, 5, 65
Gupta, A., & Schlichting, H. E. 2019, MNRAS, 487, 24
Gupta, A., & Schlichting, H. E. 2020, MNRAS, 493, 792
Ho, C. S. K., Rogers, J. G., Van Eylen, V., Owen, J. E., & Schlichting, H. E. 2024, MNRAS, 531, 3698
Horn, H. W., Prakapenka, V., Chariton, S., Speziale, S., & Shim, S. H. 2023, PSJ, 4, 30
Howard, A. W., Marcy, G. W., Bryson, S. T., et al. 2012, ApJS, 201, 15
Hunten, D. M., Pepin, R. O., & Walker, J. C. G. 1987, Icar, 69, 532
Jontof-Hutter, D., Lissauer, J. J., Rowe, J. F., & Fabrycky, D. C. 2014, ApJ, 785, 15
Joselyn, J., & Holzer, T. E. 1978, JGR, 83, 1019
Karki, B. B., Wentzcovitch, R. M., de Gironcoli, S., & Baroni, S. 2000, PhRvB, 62, 14750
Kite, E. S., Fegley, B., Schaefer, L., & Gaidos, E. 2016, ApJ, 828, 80
Kite, E. S., Fegley, B., Schaefer, L., & Ford, E. B. 2019, ApJL, 887, L33
Kite, E. S., Fegley, B., Schaefer, L., & Ford, E. B. 2020, ApJ, 891, 111
Kite, E. S., & Schaefer, L. 2021, ApJL, 909, L22
Kubyshkina, D., & Fossati, L. 2022, A&A, 668, A178
Lam, K. W. F., Csizmadia, S., Astudillo-Defru, N., et al. 2021, Sci, 374, 1271
Lee, E. J., Chiang, E., & Ormel, C. W. 2014, ApJ, 797, 95
Lichtenberg, T. 2021, ApJL, 914, L4
Lopez, E. D., & Fortney, J. J. 2013, ApJ, 776, 2
Lopez, E. D., & Fortney, J. J. 2014, ApJ, 792, 1
Luger, R., & Barnes, R. 2015, AsBio, 15, 119
Madhusudhan, N., Sarkar, S., Constantinou, S., et al. 2023, ApJL, 956, L13
Markham, S., Guillot, T., & Stevenson, D. 2022, A&A, 665, A12
Misener, W., & Schlichting, H. E. 2021, MNRAS, 503, 5658
Misener, W., & Schlichting, H. E. 2022, MNRAS, 514, 6025
Misener, W., Schlichting, H. E., & Young, E. D. 2023, MNRAS, 524, 981
Moore, G., Vennemann, T., & Carmichael, I. S. E. 1998, AmMin, 83, 36
Mulders, G. D., Pascucci, I., Apai, D., & Ciesla, F. J. 2018, AJ, 156, 24
Murray-Clay, R. A., Chiang, E. I., & Murray, N. 2009, ApJ, 693, 23
Olson, P., & Sharp, Z. D. 2018, E&PSL, 498, 418
Otegi, J. F., Bouchy, F., & Helled, R. 2020, A&A, 634, A43
Owen, J. E., & Campos Estrada, B. 2020, MNRAS, 491, 5287
Owen, J. E., & Jackson, A. P. 2012, MNRAS, 425, 2931
Owen, J. E., & Lai, D. 2018, MNRAS, 479, 5012
Owen, J. E., & Schlichting, H. E. 2024, MNRAS, 528, 1615
Owen, J. E., & Wu, Y. 2013, ApJ, 775, 105
Owen, J. E., & Wu, Y. 2016, ApJ, 817, 107
Owen, J. E., & Wu, Y. 2017, ApJ, 847, 29
Petigura, E. A., Rogers, J. G., Isaacson, H., et al. 2022, AJ, 163, 179
Piet, H., Chizmeshya, A., Chen, B., et al. 2023, GeoRL, 50, e2022GL101155
Rafikov, R. R. 2006, ApJ, 648, 666
Rogers, J. G., Gupta, A., Owen, J. E., & Schlichting, H. E. 2021, MNRAS, 508, 5886
Rogers, J. G., Janó Muñoz, C., Owen, J. E., & Makinen, T. L. 2023a, MNRAS, 519, 6028
Rogers, J. G., & Owen, J. E. 2021, MNRAS, 503, 1526
Rogers, J. G., Owen, J. E., & Schlichting, H. E. 2024, MNRAS, 529, 2716
Rogers, J. G., Schlichting, H. E., & Owen, J. E. 2023b, ApJL, 947, L19
Rogers, L. A. 2015, ApJ, 801, 41
Rogers, L. A., & Seager, S. 2010, ApJ, 712, 974
Salvador, A., & Samuel, H. 2023, Icar, 390, 115265
Schlichting, H. E., & Young, E. D. 2022, PSJ, 3, 127
Schulik, M., & Booth, R. 2023, MNRAS, 523, 286
Seager, S., Kuchner, M., Hier-Majumder, C. A., & Militzer, B. 2007, ApJ, 669, 1279
Silburt, A., Gaidos, E., & Wu, Y. 2015, ApJ, 799, 180
Stixrude, L. 2014, RSPTA, 372, 20130076
Suer, T.-A., Jackson, C., Grewal, D. S., Dalou, C., & Lichtenberg, T. 2023, FrEaS, 11, 1159412
Trierweiler, I. L., Doyle, A. E., & Young, E. D. 2023, PSJ, 4, 136
Van Eylen, V., Agentoft, C., Lundkvist, M. S., et al. 2018, MNRAS, 479, 4786
Virtanen, P., Gommers, R., Oliphant, T. E., et al. 2020, NatMe, 17, 261
Weiss, L. M., & Marcy, G. W. 2014, ApJ, 783, L6
Wogan, N. F., Batalha, N. E., Zahnle, K., et al. 2024, ApJL, 963, L7
Wood, B. J. 2008, RSPTA, 366, 4339
Wu, Y. 2019, ApJ, 874, 91
Xiang, Y., Sun, D. Y., Fan, W., & Gong, X. G. 1997, PhLA, 233, 216
Young, E. D., Shahar, A., & Schlichting, H. E. 2023, Natur, 616, 306
Zahnle, K. J., & Kasting, J. F. 1986, Icar, 68, 462
Zhang, J., & Rogers, L. A. 2022, ApJ, 938, 131
Zink, J. K., Christiansen, J. L., & Hansen, B. M. S. 2019, MNRAS, 483, 4479